Thin-Walled Structures 132 (2018) 549–557

Contents lists available at ScienceDirect

Thin-Walled Structures

journal homepage: www.elsevier.com/locate/tws

Full length article

# On similarity criteria of thin-walled cylinder subjected to complex thermomechanical loads

Te Ma[a,b,c], Xiaodong Xing[c], Hongwei Song[a,b,*], Chenguang Huang[a,b]

[a] Key Laboratory for Mechanics in Fluid-Solid Coupling Systems, Institute of Mechanics, Chinese Academy of Sciences, Beijing 100190, China
[b] School of Engineering Science, University of Chinese Academy of Sciences, Beijing 100049, China
[c] Harbin Engineering University, Harbin 150000, China

ARTICLE INFO

*Keywords:*
Similarity criteria
Thin-walled cylinder
Thermomechanical loads
Thermal elastoplastic
Buckling
Dynamic rupture

## 1. Introduction

Thin-walled cylinders have been widely applied in many industrial sectors. In-depth theoretical analysis, systematic experimental research, and finite element analysis (FEA) have been conducted on various aspects of the cylindrical shell, such as the critical buckling load of the cylindrical shell under axial compression [1–6], the influence of laser irradiation on the critical buckling load of the axially compressed cylindrical shell [7,8], the failure mode, the corresponding damage threshold and the damage law of the internally pressurized cylindrical shell under laser irradiation [9–16]. In the analysis process, many factors have considerable influence on the thermomechanical damage behaviors, including the material properties, the geometry of the cylindrical shell, the initial geometric and loading imperfection, the internal pressure, and parameters of the laser beam. Comprehensive experiments may be difficult to accomplish because experiments with the prototype structure are time-consuming and costly. Only a few trials can be used for identification experiments, and many scaled model tests are used to validate numerical models and obtain laws of influencing factors, which involve the problems of scaling laws and similarity criteria. From an objective perspective, similarity criterion is a relatively mature scientific research tool, which was finalized in the 1950s, and its wide applications have led to great achievements in fluid mechanics, aerodynamics, mechanics of explosion and other mechanical problems [17–19]. Liu et al. [20] studied the similarity criteria on the thermal protection system (TPS) of a high-speed aircraft, which could be designed according to the test type with a high degree of flexibility. Stephen et al. [21] presented a set of four independent similarity criteria that must be satisfied on the scaling solar sail systems. Torkamani et al. [22] used the Donnell-type nonlinear strain-displacement relations along with the smearing theory and the similitude theories to develop the necessary similarity conditions, or scaling law, for free vibrations of orthogonally stiffened cylindrical shells. De Rosa et al. [23] investigated the definition and applicability of distorted similitudes and the related scaling laws for the analysis of the dynamic forced response of rectangular composite plates. Asl et al. [24] demonstrated the applicability of structural similitude theory in designing partially similar composite structures. Yazdi et al. [25] investigated the flutter pressure of delaminated composite beam–plate subjected to supersonic flow by using similitude theory. Moreover, a procedure has been developed to demonstrate the use of these similarity criteria in designing a model for ground testing. The similarity criterion also plays a significant role in the study of failure mechanisms of laser irradiated cylindrical shell with internal pressure. Huang et al. [26] derived a similarity criterion based on dimensional analysis methods, and verified it through numerical calculation.

In practical applications, the structural integrity of a cylindrical shell is determined by coupling loads of laser irradiation, axial compression and internal pressure. In this load-function situation, obtaining a theoretical or analytical solution for the complex thermal elastoplastic

* Corresponding author at: Key Laboratory for Mechanics in Fluid-Solid Coupling Systems, Institute of Mechanics, Chinese Academy of Sciences, Beijing 100190, China.
*E-mail address:* songhw@imech.ac.cn (H. Song).

https://doi.org/10.1016/j.tws.2018.09.015
Received 9 January 2018; Received in revised form 5 August 2018; Accepted 4 September 2018
Available online 19 September 2018
0263-8231/ 

damage behavior is difficult. Experimental results of the model obtained by scaling the prototype structure and the similarity criteria are used to estimate the true structural damage model, damage threshold, or structural response, thereby providing effective data for cylindrical shells in a preliminary design stage. However, the similarity criteria of thin-walled cylinders under such complex coupling loads have not been developed so far.

In this study, dimensionless processing is conducted in governing equations, i.e., heat conduction equation, equilibrium equation and thermal elastoplastic constitutive equation, and the similarity criteria are obtained for cylindrical shells subjected to coupled thermo-mechanical loads or an individual load. Finite element models and systemic methods are established to simulate the coupled behavior of the thermal response, dynamic rupture, and buckling response of the cylindrical shell, and the numerical models are validated with experiments. Finally, scaled numerical models are utilized to validate the similarity criteria, and the error sources of the scaling law are analyzed.

## 2. Methodology

### 2.1. Governing equations

Heat conduction controls the heat transfer in the structure. In Cartesian coordinates, the coupled heat conduction equations for isotropic thermal elastoplastic material is expressed as follows:

$$\rho C\frac{\partial T}{\partial t} = \frac{\partial}{\partial x_i}\left(k\frac{\partial T}{\partial x_i}\right) + \rho\gamma - \frac{E}{1-2\upsilon}T_\varepsilon\dot{\varepsilon}_{kk} + \dot{Q}_p \tag{1}$$

where $\rho$ is the density; $C$ is the specific heat capacity; $T$ is the temperature; $t$ is the time; $k$ is the thermal conductivity; $\gamma$ is the heat generation rate of unit mass; $-ET_\varepsilon\dot{\varepsilon}_{kk}/(1-2\upsilon)$ is an additional term for the internal heat source, which indicates heat generation when $\dot{\varepsilon}_{kk} < 0$ (compression) and heat absorption when $\dot{\varepsilon}_{kk} > 0$ (expansion); $\dot{Q}_p$ is inelastic heating, which is the difference between the plastic power and the change rate of the internal energy of cold work. Ignoring the coupling term yields, we obtained

$$\frac{\partial T}{\partial t} = \frac{k}{\rho C}\nabla^2 T + \frac{\gamma}{C} \tag{2}$$

where $\nabla^2$ is the Laplace operator, $\left(\frac{\partial^2}{\partial x^2}+\frac{\partial^2}{\partial y^2}+\frac{\partial^2}{\partial z^2}\right)() = \nabla^2()$.

The thermal boundary condition in the laser irradiation region is expressed as follows:

$$-k\frac{\partial T}{\partial x_i} = \chi Q + h(T_w - T_\infty) + \varepsilon\sigma T_w^4 \tag{3}$$

where $\chi$ is the absorption coefficient; $Q$ is the laser power density; $h$ is the convective heat transfer coefficient; $T_w$ is the surface wall temperature; $T_\infty$ is the environment temperature; $\varepsilon$ is the emissivity; $\sigma$ is the Stefan-Boltzmann constant. In this study, the heat flux from the forced convection and thermal radiation is negligible compared with that of the laser source (typically $10^4$ W/m$^2$ vs $10^6$ W/m$^2$). Therefore, the boundary condition of the surface irradiated with laser is transformed into

$$k\frac{\partial T}{\partial x_i} = \chi Q \tag{4}$$

The stress field can be described by the three-dimensional perfect thermal elastoplastic equations.

$$\text{Equilibrium equation: } \sigma_{ij,j} + f_i = 0 \tag{5}$$

$$\text{Geometric equation: } \varepsilon_{ij} = \varepsilon_{ij}{}^e + \varepsilon_{ij}{}^p = \frac{1}{2}(u_{i,j}{}^e + u_{j,i}{}^e) + \frac{1}{2}(u_{i,j}{}^p + u_{j,i}{}^p) \tag{6}$$

$$\text{Constitutive equation: } \sigma_{ij} = \lambda(T)\varepsilon_{kk}\delta_{ij} + 2G(T)(\varepsilon_{ij} - \varepsilon_{ij}{}^p) - \frac{E}{1-2\upsilon}\alpha T\delta_{ij} \tag{7}$$

where $\sigma_{ij}$ is the stress; $f$ is the body force; $\varepsilon_{ij}$ is the total strain; $\varepsilon_{ij}^e$ is the elastic strain; $\varepsilon_{ij}^p$ is the plastic strain; $u_{ij}^e$ is the deformation in the elastic range; $u_{ij}^p$ is the deformation in the plastic range; $\lambda$ and $G$ is the Lame constant; $E$ is Young's modulus; $\upsilon$ is Poisson's ratio; and $\alpha$ is the coefficient of linear expansion.

The above equilibrium and geometric equations are introduced into the constitutive equation, and the transformation form can be obtained as shown in Eq. (8).

$$f_i = \begin{array}{l}\frac{E}{2(1+\upsilon)}\nabla^2 u_i + \frac{E}{2(1+\upsilon)}\nabla^2 u_i^p \\ + \frac{E}{2(1-2\upsilon)(1+\upsilon)}\frac{\partial\theta}{\partial i} - \frac{E\alpha}{1-2\upsilon}\frac{\partial T}{\partial i}\end{array} \tag{8}$$

where $\theta = \frac{\partial u}{\partial x} + \frac{\partial v}{\partial y} + \frac{\partial w}{\partial z}$.

The equation for the volume force of a cylindrical shell subjected to axial compression and internal pressure is

$$f = \frac{F}{V}; f = \frac{PA}{V} \tag{9}$$

where $F$ is the axial compression; $V$ is the cylindrical shell volume; $P$ is the internal pressure; and $A$ is the surface area of the shell wall.

### 2.2. Dimensionless transformation

Defining the dimensionless parameters: $T_0 = T/T'$; $t_0 = t/t'$; $u_0 = u/u'$; $\theta_0 = \theta/\theta'$; $\gamma_0 = \gamma/\gamma'$; $f_0 = f/f'$; $Q_0 = Q/Q'$; $F_0 = F/F'$; $P_0 = P/P'$; $k_0 = k/k'$; $\rho_0 = \rho/\rho'$; $C_0 = C/C'$; $\chi_0 = \chi/\chi'$; $E_0 = E/E'$; $\upsilon_0 = \upsilon/\upsilon'$; $\alpha_0 = \alpha/\alpha'$. And $l_0$ is the characteristic length of the model, and it can be regarded as the intrinsic characteristic of the model. Thus, Eqs. (2), (4), (8), and (9) are transformed into dimensionless forms.

$$\begin{cases} \frac{\partial T'}{\partial t'} = \frac{k' k_0 t_0}{\rho' \rho_0 C' C_0 l_0{}^2}\nabla^2 T' + \frac{t_0\gamma_0}{C' C_0 T_0}\gamma'; \\ k\frac{\partial T'}{\partial x_i'} = \chi'\chi_0\frac{l_0}{T_0}Q_0 Q'; \\ f_0 l_0 f'_i = \begin{array}{l}\frac{E' E_0}{2(1+\upsilon'\upsilon_0)}\frac{u_0}{l_0}\nabla^2 u'_i + \frac{E' E_0}{2(1+\upsilon'\upsilon_0)}\frac{u_0^p}{l_0}\nabla^2 u'^p_i \\ + \frac{E' E_0}{2(1-2\upsilon'\upsilon_0)(1+\upsilon'\upsilon_0)}\theta_0\frac{\partial\theta'}{\partial l'} - \frac{E' E_0}{1-2\upsilon'\upsilon_0}\alpha'\alpha_0 T_0\frac{\partial T'}{\partial l'}; \end{array} \\ f'_i = \frac{F_0 F'}{f_0 l_0{}^3 l'^3}; f'_i = \frac{P_0 P'}{f_0 l_0 l'}; \end{cases} \tag{10}$$

The coefficients of each variable in the equations should be unified to ensure the similarity of physical problems. Given that the problem does not involve the phase change of the material, unifying the coefficients in the dimensionless equation (Eq. (10)) and corresponding equations (Eqs. (2), (3), (7), and (8)), $\theta_0$ and $T_0$ should be equal to 1. Therefore, the strain and temperature fields for the two similar physical problems remain unchanged. On the basis of these assumptions, the other coefficients in Eq. (10) are derived and simplified. Table 1 presents the similarity criteria and physical explanations. These coefficients should remain unchanged to maintain the scaling law.

### 2.3. Scaling laws

On the basis of the dimensionless transformation and similarity criteria obtained in Section 2.2, the geometric dimensions of the cylindrical shell (including the laser spot size) are scaled by $\beta$ times, Table 2 shows the scaling ratio of the relative physical parameters.

The physical parameters can be divided approximately into thermomechanical loads and responses. The thermomechanical loads include laser irradiation time, laser power density, axial compression force, and internal pressure. Meanwhile, the thermomechanical response includes the temperature and strain fields. The thermomechanical response (i.e., temperature and strain fields) must remain unchanged when scaling the geometry of the cylindrical shell. As shown

**Table 1**
Similarity criteria and guidelines.

| No. | Similarity criteria | Physical explanation |
|---|---|---|
| 1 | $t_0/l_0^2$ | The simplification of the Fourier number : $a_0\ t_0\ /\ l_0^2$, where $a_0$ is thermal diffusivity, when the material phase remains unchanged, the term is the ratio of the laser irradiation time to the square of the geometric dimension is unchanged |
| 2 | $t_0\gamma_0$ | The laser irradiation time is multiplied by the heat generation rate of unit mass |
| 3 | $l_0 Q_0$ | The laser power density is multiplied by geometric size |
| 4 | $u_0/l_0$ | The deformation field is divided by the geometric dimension |
| 5 | $f_0 l_0$ | The body force is multiplied by the geometric dimension |
| 6 | $F_0/l_0^2$ | The compressive load is divided by the square of the geometric dimension |
| 7 | $P_0$ | The internal pressure is unchanged |

in Table 2, when the dimension is scaled by $\beta$, the laser power density and laser irradiation time should be scaled by $1/\beta$ and $\beta^2$, respectively; the compression load should be scaled by $\beta^2$, and the internal pressure remains unchanged.

## 3. Numerical models and experimental validations

### 3.1. Outline of the flowchart

The failure behavior of the cylindrical shell subjected to the combined loads of axial compression and internal pressure under laser irradiation is a coupling problem of thermal elastoplastic dynamics. The numerical simulation of this problem involves a comprehensive process, including heat conduction, thermal stress, elastoplastic buckling, and dynamic rupture failure, with strong characteristics of geometric and material nonlinearities. The specific flowchart is shown in Fig. 1. The pink module is the heat conduction analysis, the green module is the prestressed field calculation of the cylindrical shell subjected to the combined loads of axial compression and internal pressure, and the blue module is the coupling calculation and failure analysis. The flowchart has two points that need to be addressed. First, the initial geometric imperfection is an important factor for the analysis when the cylindrical shell is subjected to axial compression. Second, the critical value of the failure criterion is the main parameter for simulating the dynamic expansion and rupture process of the internally pressurized cylindrical shell under laser irradiation.

The following assessment schemes are presented to validate the established approach and similarity criterion. Case 1 is concerned with the temperature field, thermal stress, and thermal strain fields induced by the laser. Case 2 is concerned with the axially compressed cylindrical shell under laser irradiation. Case 3 is concerned with the internally pressurized cylindrical shell under laser irradiation. Case 4 is concerned with the cylindrical shell subjected to the combined loads of axial compression and internal pressure under laser irradiation.

The scaling ratio of $\beta = 1/2$ is adopted in the four cases when validating the similarity criterion. Therefore, in each case, two numerical models are built, namely, Model-1 and -2. Model-1 is the prototype with the dimensions of $L_1$ (length) = 1 m, $D_1$ (neutral surface diameter) = 0.54 m, and $d_1$ (thickness) = 0.005 m. Model-2 is the prediction model with the dimensions of $L_2$ = 0.5 m, $D_2$ = 0.27 m, and $d_2$ = 0.0025 m. The number of elements in the FEA model is 16600, and the element type is S4R. Specific cases determined the boundary conditions.

### 3.2. Case 1: thermal–structural model for laser irradiation

When the laser irradiates the metallic cylindrical shell, the laser energy absorbed by the surface layer will diffuse in the cylindrical shell in the form of heat conduction, and partially dissipate outward by radiation and convection. The heat loss can be considered in the value of the laser absorption coefficient. When the input laser power density is considerably larger than the output heat flux due to radiation and convection, the effects of radiation and convection can be negligible. When temperature increases, the mechanical properties of materials, such as elastic modulus and yield strength, become significantly lower than those at room temperature. Thermal parameters, such as specific heat, thermal expansion coefficient, and thermal conductivity, also undergo changes. An uneven temperature increase can result in thermal stress. Thermal stress analysis methods can be divided into two categories in FEA, this is, direct and sequential thermal mechanical coupling. In the direct thermomechanical coupling analysis, the temperature field directly affects the structural stress field, and the structural deformation influences the temperature field. In the sequential thermomechanical coupling analysis, the influence of deformation field on the temperature field is ignored, and the analysis is divided into two processes, that is, heat transfer and thermal stress analyses. According to the analysis of heat conduction in Section 2.1, the temperature field coupling term caused by the structural deformation is neglected, and then simplified as the sequential thermal mechanical coupling. The material used in the thin-walled cylindrical shell is an extra super duralumin alloy, which is an ideal thermal elastoplastic material, Table 3 lists the thermomechanical parameters of the material at different temperatures.

The maximum temperature, thermal stress, and thermal strain produced by laser irradiation in Model-1 are consistent with those of Model-2 only when the laser parameters satisfy the similarity criteria Nos. 1, 2 and 3 mentioned in Table 1. The laser beam parameters of Models-1 and -2 are respectively shown as follows: the laser power densities are $Q_1$ = 38.2 W/cm$^2$ and $Q_2$ = 76.4 W/cm$^2$; the laser spot radii are $r_1$ = 5 cm and $r_2$ = 2.5 cm, and the laser irradiation times are $t_1$ = 40 s and $t_2$ = 10 s. The initial temperature is $T_1 = T_2$ = 293 K, and the spatial distribution of the laser is uniform(Gauss).

### 3.3. Case 2: buckling model for the axial compression-induced damage

Two different imperfection techniques, namely, eigenmode–affine method and single perturbation load approach (SPLA), are adopted in the critical buckling load of the cylindrical shell with initial imperfection under axial compression in FEA. The eigenmode–affine method generally provides conservative buckling load prediction. The critical buckling loads predicted by the SPLA are in good agreement with the published experimental data, thereby making it a popular algorithm for the preliminary design of cylindrical shells in calculating critical buckling loads [3]. However, the SPLA is not applicable when studying the influence of laser irradiation on the buckling behavior of thin-

**Table 2**
Scaling ratio of the cylindrical shells under multiple loads.

| | Thermomechanical responses | | | Thermomechanical loads | | | |
|---|---|---|---|---|---|---|---|
| | Deformation | Temperature | Strain field | Irradiation time | Laser power density | Axial compression | Internal pressure |
| Parameters | $\mu_0$ | $T_0$ | $\theta_0$ | $t_0$ | $Q_0$ | $F_0$ | $P_0$ |
| Scaling | $\beta$ | 1 | 1 | $\beta^2$ | $1/\beta$ | $\beta^2$ | 1 |

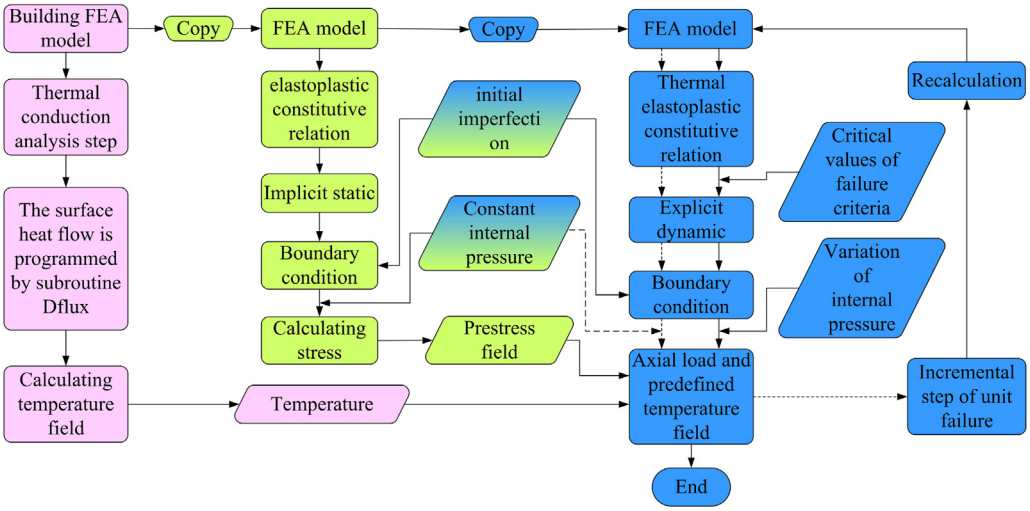


**Fig. 1.** Flowchart of numerical simulation.

**Table 3**
Thermomechanical parameters of the extra super duralumin alloy at different temperatures.

| $T$ / K | $k$ /(W·m$^{-1}$·K$^{-1}$) | $C$ /(J·kg$^{-1}$·K$^{-1}$) | $\alpha$ /(10$^{-6}$·K$^{-1}$) | $E$ /GPa | $\sigma_s$ /MPa |
|---|---|---|---|---|---|
| 293 | 155 | 880 | 22 | 66 | 432 |
| 373 | 159 | 921 | 23.6 | 61 | 402 |
| 473 | 163 | 1005 | 25.2 | 50 | 235 |
| 573 | 163 | 1047 | 26.8 | 46 | 118 |
| 673 | 159 | 1089 | 28.4 | 43 | 69 |

walled cylindrical shells. Laser irradiation is a complex perturbation load that reduces the strength of local materials which leads to the thermal expansion of the cylindrical shell. This type of load conflicts with SPLA. Therefore, the introduction of the initial imperfection adopts the eigenmode–affine method in the present models, and its feasibility is verified by corresponding experimental results.

Given the thermal boundary condition in the laser irradiation region, the cooling effects of convection and radiation will lead to the thermal equilibrium of the temperature field when the laser power density is low. Therefore, the buckling of the experiment scheme is as follows. First, the cylindrical shell specimen is placed in the material testing machine (MTS) fixture; The specimen is then subjected to laser irradiation in the center of the cylindrical shell for 200 s until the thermal equilibrium is established. Finally, axial compression is applied through MTS until the specimen is buckled. In the experiment, the dimensional scaling ratio $\beta = 1/10$ is adopted, that is, the diameter is $D = 54$ mm and wall thickness is $t = 0.5$ mm. Each side of the specimen wall is thickened to 1 mm with a section length of 12 mm to avoid accidental premature failure of the specimen. The axial compression loading rate is controlled at 0.5 mm/min. On the basis of the experimental conditions, the quasi-static analysis is conducted in the dynamic explicit analysis module. Table 4 shows the comparison of the critical buckling load obtained by the experiments and predicted by the numerical model, and Fig. 2 shows the comparison of the compressive load versus end-shortening curves and buckling modes.

**Table 4**
Critical buckling load obtained by the experiments and FEA.

| | Critical buckling load without incident laser $F_{cr}$ (kN) | Critical buckling load with incident laser $F_{crl}$ (kN) | $F_{crl}/F_{cr}$ |
|---|---|---|---|
| Experiment | 24.1 | 12.8 | 0.53 |
| FEA | 27.6 | 14.1 | 0.51 |

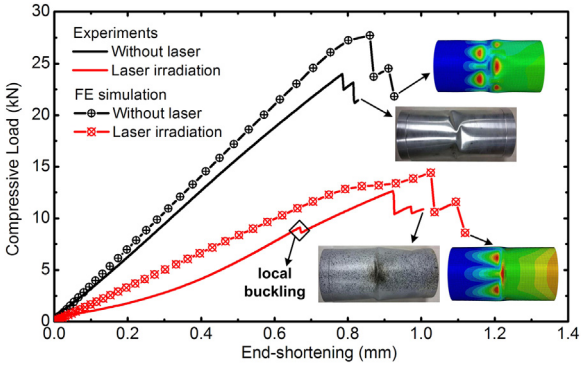


**Fig. 2.** Comparison of the buckling modes and compressive load versus end-shortening curves obtained by the experiments and finite element simulation.

The error of the critical buckling load using the eigenmode–affine method compared with the experimental result is 14.5% in the absence of incident laser irradiation and 10.1% with laser irradiation, as shown in Table 4. The error of the laser knockdown factor ($F_{crl}/F_{cr}$) is 3.8%. The above data indicate that the critical buckling load obtained by the eigenmode–affine method is conservative without perturbation load. Conversely, the error is reduced when the perturbation load is imposed, and the error of the laser impact factor is only 3.8%. As shown in Fig. 2, the buckling mode obtained by the numerical calculation is basically consistent with the experimental result. Wrinkling occurs locally in the laser spot region in the experimental and numerical simulation results when laser irradiation is employed. This finding explains the influence of laser irradiation on the buckling behavior of the cylindrical shell.

The axial compression loading should satisfy the similarity criteria Nos.5 and 6 in Table 1 to validate of damage behavior of axially compressed cylindrical shell under laser irradiation. The total displacement load and all parameters in the experiment are expanded to Models-1 and -2 according to the scaling laws.

### 3.4. Case 3: dynamic rupture model for internal pressure–induced damage

The rupture damage behavior of laser–induced internally pressurized cylindrical shell has been investigated in the literature. The difficulty still lies in the FEA because no universally recognized criterion for the thermal elastoplastic fracture under laser irradiation is available. Therefore, simulating the dynamic rupture process of the internally pressurized cylindrical shell is rather difficult. In the present study, the

critical value of failure criterion is selected by comparing the ultimate internal pressure obtained via theoretical calculation and the internal pressure under the failure of the cylindrical shell obtained via numerical simulation. The secondary development subroutine is used in optimizing the failure mode to simulate the leakage pressure of the cylindrical shell. When the increment step reaches the corresponding value of the damage, the pressure inside the shell is rapidly decreases to zero.

For the thick-walled cylinder with internal pressure, the stress equation is obtained by simultaneously solving the deformation geometric condition, static equilibrium equation and physical equation, as shown as follows:

$$\left.\begin{matrix}\sigma_r\\ \sigma_\theta\end{matrix}\right\} = \frac{P_1}{b^2 - a^2}\left(1 \mp \frac{b^2}{r^2}\right) \tag{11}$$

where $\sigma_r$ is the radial stress; $\sigma_\theta$ is the hoop stress; $P_1$ is the internal pressure; $a$ is the inner wall radius; $b$ is the outer wall radius, and $r$ is any radius of the wall thickness.

For the thin-walled cylindrical shell, the wall thickness $d = b - a$ is considerably smaller than radii $a$ and $b$, and it can be reasonably approximated by $b^2/r^2 + 1 \approx 2$ and $b^2 - a^2 = (b - a)(b + a) \approx dD$, Eq. (11) is then converted to

$$\sigma_\theta = \frac{P_1 D}{2d} \tag{12}$$

The ultimate internal pressure $P_d$ of an ideal thin-walled cylindrical shell can be obtained according to the Mises flow condition.

$$P_d = \frac{2t\sigma_s}{D} \tag{13}$$

The failure criterion of the maximum equivalent plastic strain is then used in FEA, and the threshold of the failure criterion is explored according to the ultimate internal pressure solved by Eq. (13). Accordingly, the critical failure value of each temperature field during laser irradiation is obtained.

To verify the above method, the numerical model of the parameters consistent with the relevant experiment [27] is established. Fig. 3 shows the failure modes of the column shell predicted by the numerical model and obtained by the experiment. The fractured crack propagates along the axis, and then bifurcates in the near end due to geometrical constraint conditions and stress concentration, and finally tears the specimen apart. The predicted damage time is 1.1 s, whereas the experimental measured damage time is 1.3 s.

The similarity criterion shows that the stress and strain fields of the structure under the same temperature are consistent when the laser parameters and internal pressure conform to the similarity criteria (Nos. 1, 2, 3 and 4). Therefore, the critical value of the failure criteria introduced in Model-1 must be identical with that in Model-2. The specific parameters in the assessment scheme of the similarity criterion are as follows. The internal pressure is $P_1 = P_2 = 5$ MPa, and the temperature field obtained in Sections 3.2 is applied in the models.

### 3.5. Case 4: model verification under complex thermomechanical loads

On the basis of the above analysis, the sequential coupling method is adopted in the thermomechanical coupled analysis, which neglects the coupling term of the temperature field caused by structural deformation. Therefore, the temperature field can be directly iterated into the analysis step. The displacement and axial load will be in conflict with the laser irradiation, and the direct loading will introduce the inertia effect when axial compression and internal pressure must be applied in the dynamic explicit analysis. Therefore, static analysis is conducted through the implicit algorithm, and the result of the stress is considered the prestress loaded into the cylindrical shell. The end of the cylinder is loaded with the axial uniform force and internal pressure to prevent the release of the prestress.

The stress and strain fields of Model-1 are consistent with those of Model-2 under the same temperature field. The deformation field must be consistent with the similarity criterion No. 5 when the axial compression, internal pressure and laser parameters follow the similarity criteria Nos. 1, 2, 3, 4, 6, and 7 in Case 4. The parameters in the scheme are $F_1 = 1000$ kN, $P_1 = 3$ MPa, $F_2 = 250$ kN, and $P_2 = 3$ MPa. The temperature field is as obtained in Section 3.2.

## 4. Validation of scaling laws and discussions

In Case 1, the temperature field and the thermal stress and strain results are obtained, as shown in Figs. 4 and 5, respectively. The similarity criterion of the first five items listed in Table 2 is validated in this case study.

To verify that the temperature field produced by the laser meets the similarity criterion, the two points of the temperature increase curves are shown in Fig. 4(a); one is the central point in the laser irradiation zone, and the other is the point in the low-temperature zone. The maximum temperature in the high-temperature zone of Model-1 is 852 K after 40 s of laser irradiation, whereas it is 851 K for Model-2 after 10 s of irradiation, and the error is only 0.1%. The maximum temperature in the low- temperature zone is 430 K for both models. The temperature increase curves of the two points corrected by scaling law are in good agreement with the two models. Fig. 4(b) and (c) reflect the consistency of the temperature field.

Fig. 5 presents the distribution of thermal stress, thermal strain and error analysis in the axial line and the circumferential curve through the laser spot center at the end of laser irradiation. As shown in Fig. 5(a), the maximum error in the thermal stress appears on the left-side second valleys (x = 0.45 m); the thermal stresses of Model-1 and

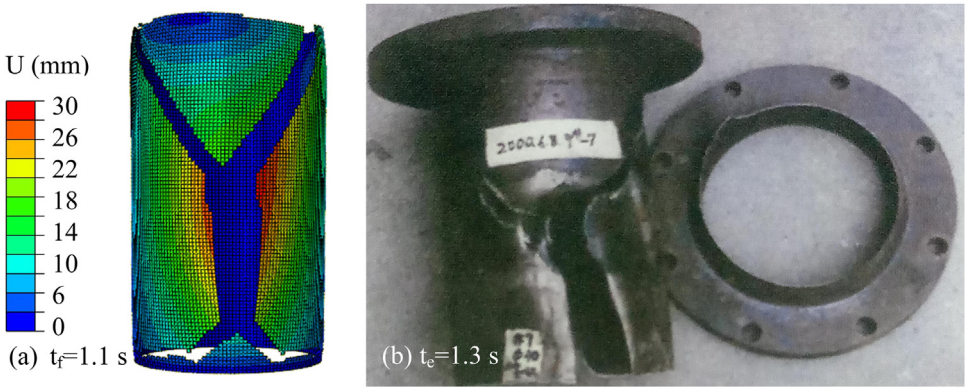


**Fig. 3.** Comparison of the rupture modes for the internally pressurized cylindrical shell irradiated by laser. (a) Numerical result. (b) Restored specimen in the experiment [27].

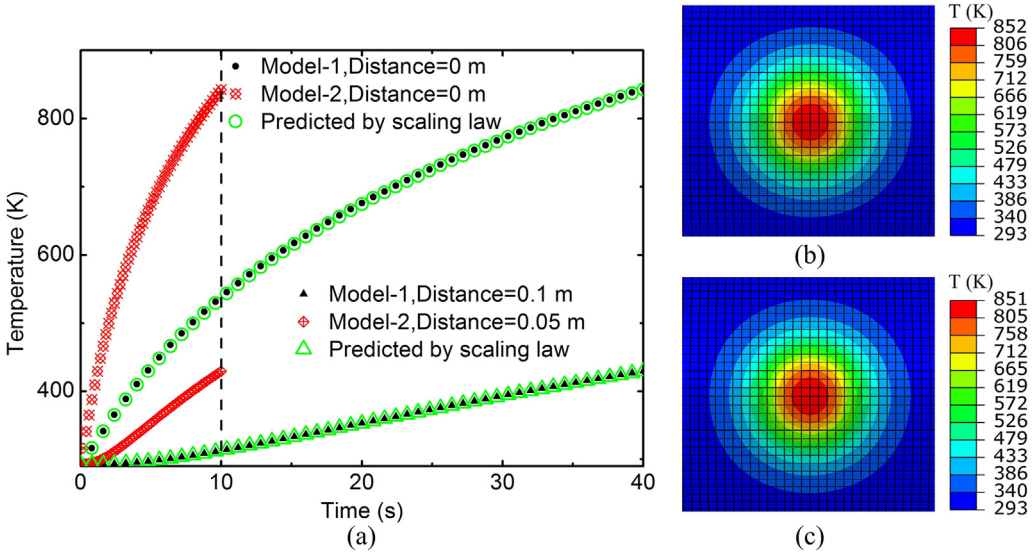


**Fig. 4.** Verification of temperature field. (a) Temperature history curves of the laser spot center and point outside the laser spot. (b) and (c) Temperature field diagrams of Model-1 and Model-2.

Model-2 are 53.1 MPa and 51.6 MPa, respectively, with an error of 2.9%. The maximum error of the thermal strain appears in the center spot (x = 0.50 m); the thermal strain of Models-1 and -2 are 0.0156 and 0.0153, respectively, with an error of 1.9%. The maximum error of thermal stress in Fig. 5(b) appears at two peaks around the spot center (y = −0.07 m and y = 0.07 m); the thermal stresses of Model-1 and Model-2 are 154.5 MPa and 152.3 MPa, respectively, with an error of 1.4%. The maximum error of the thermal strain still appears in the spot center of the laser, and the error is 1.9%. The locations where the maximum error occurs are in the high-temperature zone (851–686 K) and the middle temperature zone (686–432 K).

The errors are mainly caused by the temperature iteration error during the sequential thermomechanical coupling analysis, wherein the magnitude of the temperature increase rate is affected. Although the error is small, it still leads to plastic flow differences in the structure, thereby resulting in structural response deviation.

Figs. 6 and 7 show the results of similarity criteria in Case 2. The final deformation fields of Model-1 and Model-2 under laser irradiation are marked with the critical buckling load $F_{crl}$ (Fig. 6). The error is 0.1% after the correction of the scaling law.

Fig. 7 shows the stress and deformation fields of the cylindrical shell subjected to buckling in the axial line and the circumferential curve through the laser spot center, as well as the error analysis curve. As shown in Fig. 7(a), the maximum error in the equivalent Mises stress appears at the first trough on the right side (x = 0.62 m); the equivalent Mises stresses of Model-1 and Model-2 are 37.7 MPa and 38.3 MPa, respectively, with an error of 1.6%. The maximum deformation error occurs at the edge of the cylindrical shell (x = 0.12 m); the deformations of Model-1 and Model-2 are 0.273 mm and 0.269 mm, respectively, with an error of 1.4%. The maximum error of the equivalent Mises stress in Fig. 7(b) appears outside the temperature field (y = −0.23 m and y = 0.23 m), with 392.7 MPa and 398.2 MPa for Model-1 and Model-2, respectively, and a relative error of 1.4%. The maximum error of deformation occurs at the edge (y = −0.27 m and y = 0.27 m); the deformations are 4.571 mm and 4.612 mm for Model-1 and Model-2, respectively, with an error of 0.9%. From the error analysis curves, the maximum error of the equivalent stress and deformation do not appear in the high- temperature range; thus,

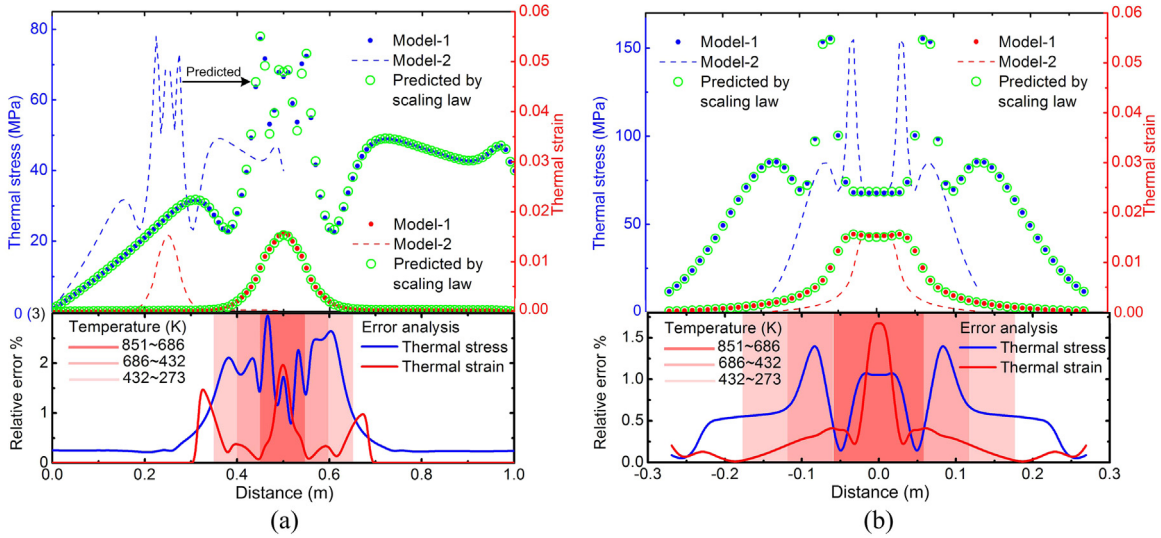


**Fig. 5.** Thermal stress and thermal strain distributions passing through the centerline of the laser spot and error analysis. (a) Axial distribution. (b) Circumferential distribution.

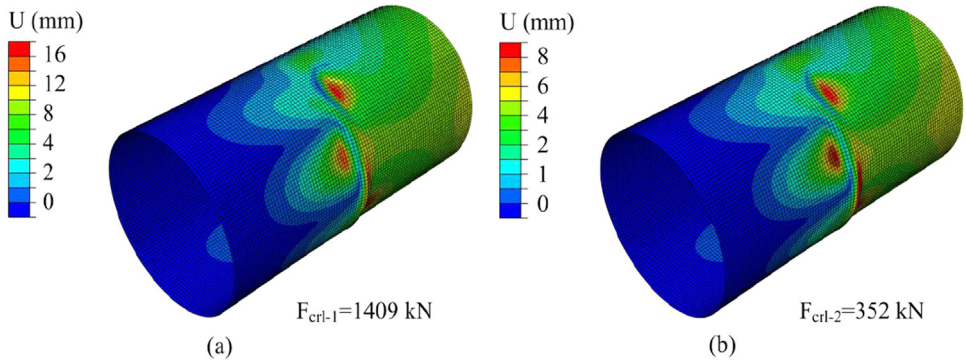


**Fig. 6.** Deformation fields of the axially compressed cylindrical shell under laser irradiation. (a) Model-1. (b) Model-2.

temperature is not the main cause of the error in Case 2. The main reason for the error may due to the inertia effect. Although the inertia effect is small and negligible, it can still lead to the structural response variance.

Figs. 8, 9 and 10 show the results of Case 3. Since this case is with strong characteristics of geometric and material nonlinearities, it is difficult to obtain an analytical result of laser irradiation. So the prestress (hoop stress) of the internally pressurized cylindrical shell without laser irradiation is given according to Eq. (12), in the FE models, as shown in Fig. 8. According to Saint-Venant principle, the normal displacement and bending internal force are both negligible when the distance to the fixed end exceeds $2.5\sqrt{Rd}$ in axisymmetric bending of cylindrical shells. Therefore, the numerical solution in the effective area is similar to the theoretical solution. Fig. 9 presents the failure mode of the internally pressurized cylindrical shell under laser irradiation and the failure time $t_d$. The errors of deformation and failure time are 3.5% and 1.4% according to the scaling law, respectively.

Fig. 10 shows the stress and the equivalent plastic strain (PEEQ) fields in the axial line and the circumferential curve through the spot center at the moment before rupture. The maximum error of the Mises stress appears in the center of the laser irradiation, as shown in Fig. 10(a). The Mises stresses of Model-1 and Model-2 are 47.8 MPa and 46.4 MPa, respectively, with an error of 2.9%. The maximum error of PEEQ is 3.3%. The maximum error of the Mises stress and PEEQ also appears around the laser spot (Fig. 10(b)). The main sources of error in Case 3 are the temperature field iteration and inertia effect.

Figs. 11 and 12 show the results of Case 4 when the cylindrical shell

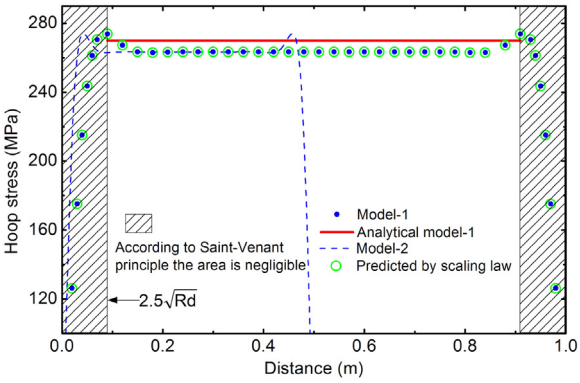


**Fig. 8.** Hoop stress distribution of the internally pressurized cylindrical shell without laser irradiation.

is subjected to the combined loads of axial compression and internal pressure under laser irradiation. The time to reach the buckling damage $t_b$ and the time to reach perforation produced by internal pressure $t_p$ are also presented in the diagram of failure modes in Fig. 11. According to the scaling law, the errors of deformation and failure time are 3.4%, 0.6% and 2.1%, respectively.

Fig. 12 illustrates the equivalent Mises stress and deformation distribution passing through the centerline of the laser spot when the cylindrical shell is subjected to the combined loads of axial compression and internal pressure under laser irradiation. The maximum error in the

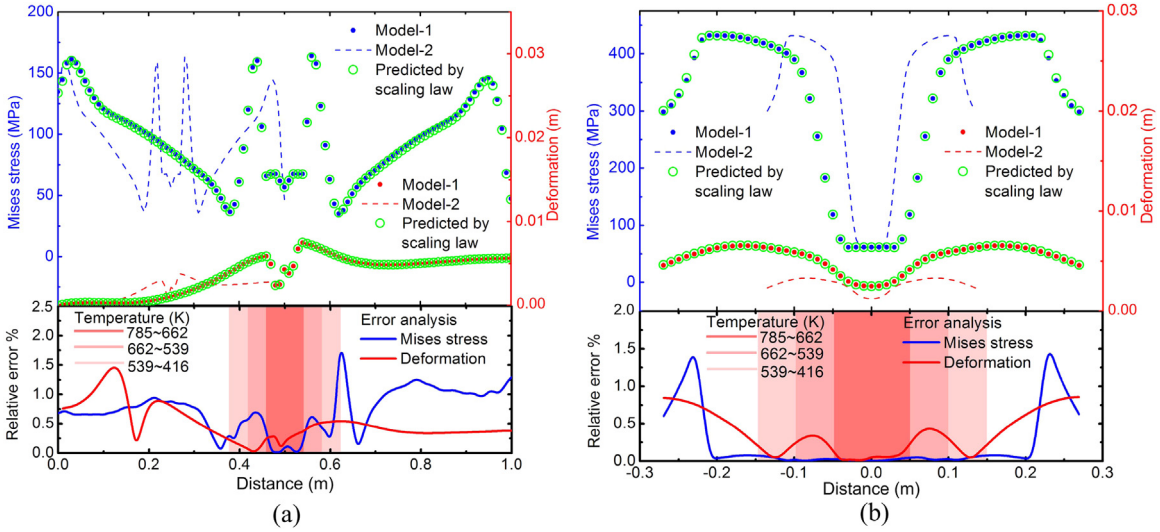


**Fig. 7.** Equivalent Mises stress and deformation distribution passing through the centerline of the laser spot and error analysis, when the axially compressed cylindrical shell under laser irradiation is buckled. (a) Axial distribution. (b) Circumferential distribution.

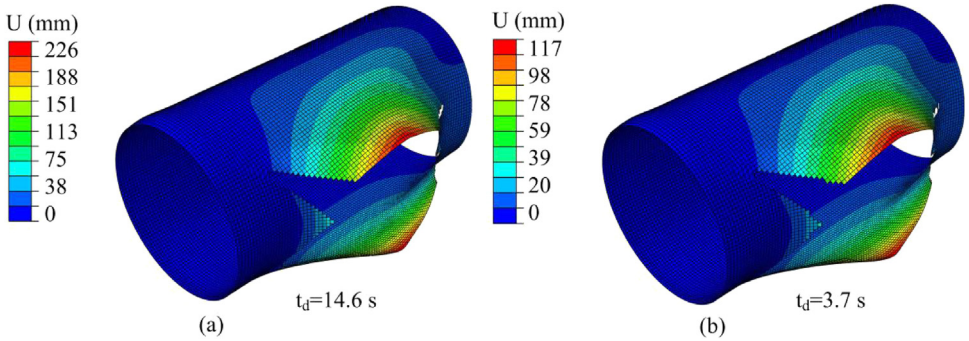


**Fig. 9.** Failure modes of internally pressurized cylinder shell under laser irradiation. (a) Model-1. (b) Model-2.

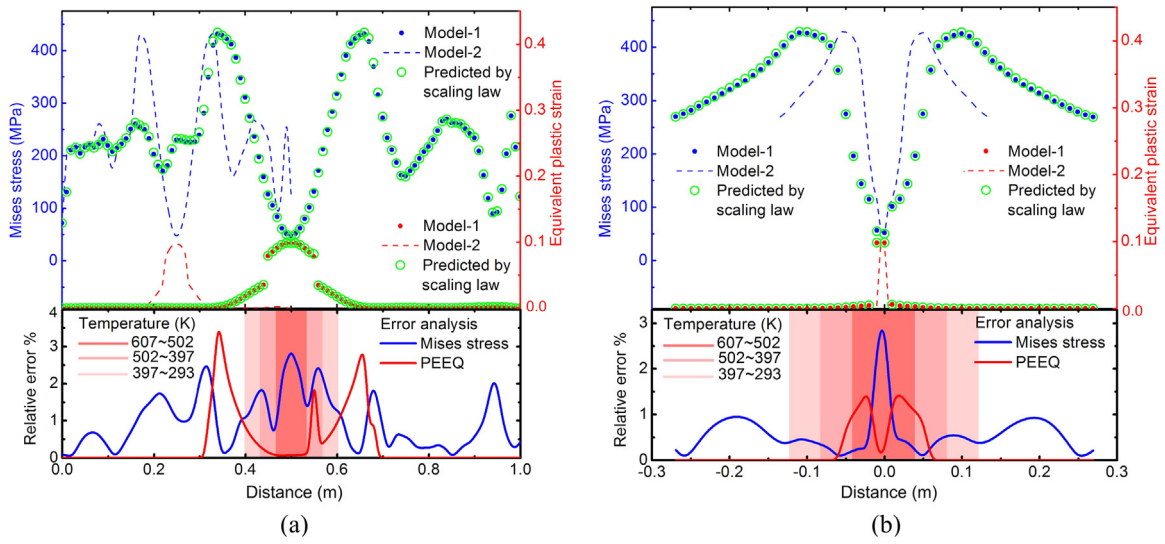


**Fig. 10.** Equivalent Mises stress and equivalent plastic strain distribution passing through the centerline of the laser spot and error analysis at the moment before rupture. (a) Axial distribution. (b) Circumferential distribution.

equivalent Mises stress appears at the second trough on the right side (x = 0.69 m); the stresses of Model-1 and Model-2 are 124.4 MPa and 130.7 MPa, respectively, with an error of 5.1%. The maximum error of deformation field appears at the beginning of the bulge (x = 0.42 m); the deformations of Model-1 and Model-2 are 0.512 mm and 0.488 mm, respectively, with an error of 1.9% (Fig. 12(a)). The maximum errors of the equivalent Mises stress and deformation field appear in the center of the spot (Fig. 12(b)). The data for the two models are 45.1 MPa and 46.2 MPa, 16.810 mm and 16.680 mm, with errors of 2.4% and 0.8%, respectively. The main sources of error in Case 4 are the combination effects of the temperature field iteration and inertia effect, which indicates that the error increases when the thermomechanical loads become highly complex.

## 5. Conclusions

This study presents similarity criteria for thin-walled cylinders subjected to coupled thermomechanical loads or individual load. Dimensionless variables and similarity criteria are derived from transforming heat conduction equations and thermal elastoplastic constitutive equations into dimensionless styles. To maintain the thermomechanical response unchanged when scaling the geometric dimension

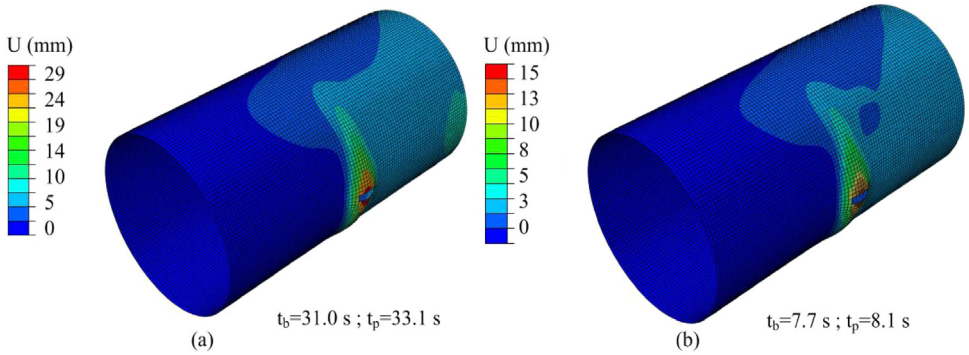


**Fig. 11.** Failure mode of the cylindrical shell subjected to the combined loads of axial compression and internal pressure under laser irradiation. (a) Model-1. (b) Model-2.

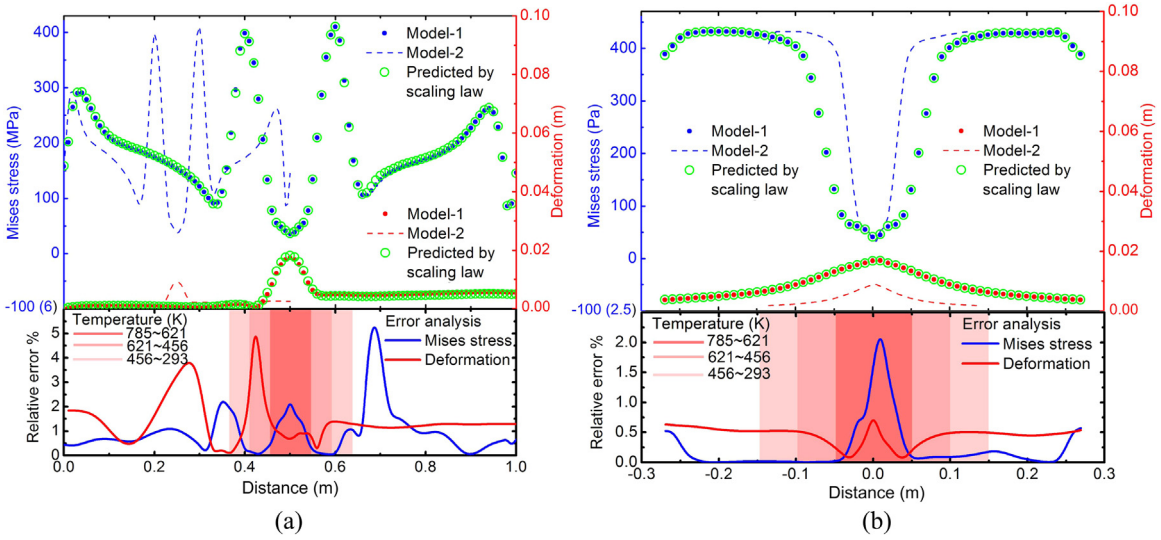


**Fig. 12.** Equivalent Mises stress and deformation distribution of the cylindrical shell subjected to the combined loads of axial compression and internal pressure under laser irradiation, and error analysis. (a) Axial distribution. (b) Circumferential distribution.

of the cylindrical shell by factor of $\beta$, the laser power density and laser irradiation time should be scaled by $1/\beta$ and $\beta^2$ and the compression load and internal pressure should be scaled by $\beta^2$ and 1, respectively. In these cases, the prototype and scaled models maintain the same temperature, strain and stress fields. Applicable methods of FEA are established according to the load situations and are verified by related experiments. Four cases are utilized to validate the similarity criteria of the laser-induced temperature, strain and stress fields; laser-induced buckling of the axially compressed cylindrical shell; laser-induced rupture of the internally pressurized cylindrical shell; and laser-induced damage under the combined loads of axial compression and internal pressure. The sources of error are also analyzed and discussed. The calculation results show that the maximum error is 5.1% in the case of stress state of the cylindrical shell under laser irradiation combined with axial compression and internal pressure. Errors in other cases are below 3.5%, indicating a reliable analysis of the similarity criterion proposed in this study. The present work provides a low cost yet convenient way to verify the structural damage model and obtain the damage threshold and structural response in the preliminary experimental stage.

## Acknowledgements

This research is supported by the National Natural Science Foundation of China under grant Nos. 11472276, 11332011 and 11502268, and National Defense Basic Scientific Research Program of China under grant No. JCKY2016130B009.

## References

[1] L.H. Donnell, C.C. Wan, Effect of imperfections on buckling of thin cylinders and columns under axial compression, J. Appl. Mech. 17 (1) (1950) 73–83.
[2] T.V. Karman, H. Tsien, The buckling of thin cylindrical shells under axial compression, J. Aeronaut. Sci. 8 (8) (1941) 303–312.
[3] M.S. Ismail, J. Purbolaksono, A. Andriyana, et al., The use of initial imperfection approach in design process and buckling failure evaluation of axially compressed composite cylindrical shells, Eng. Fail. Anal. 51 (2015) 20–28.
[4] H.N.R. Wagner, C. Hühne, S. Niemann, et al., Robust design criterion for axially loaded cylindrical shells – simulation and validation, Thin-Walled Struct. 115 (2017) 154–162.
[5] M.S. Ismail, B.T.H.T. Baharudin, Z. Talib, et al., Improvement of cylinder buckling knockdown factor through imperfection sensitivity, Adv. Mater. Res. 845 (2013) 226–230.
[6] B. Wang, K. Du, P. Hao, et al., Numerically and experimentally predicted knockdown factors for stiffened shells under axial compression, Thin-Walled Struct. 109 (2016) 13–24.
[7] K.S. Deng, Z. Ji, A.W. Davies, et al., Thermal buckling of axially precompressed cylindrical shells irradiated by laser beam, AIAA J. 38 (10) (2000) 1789–1794.
[8] Y.Z. Chen, S.Z. Li, Buckling failure of the axially pre-compressed cylindrical shell irradiated by CW CO2 laser beam, in: Proceedings of the AIAA 24th Plasmadynamics and Laser Conference, USA, 1993, Paper 93-3231.
[9] C. Sun, Y. Yuan, N. Zhang, et al., Crack formation on the cylindrical shell damaged by inner pressure and surface laser irradiation, in: Proceedings of the AIAA 30th Plasmadynamics and Laser Conference, USA, 1999, Paper 99-3548.
[10] Z. Ji, K.S. Deng, A.W. Davies, et al., Numerical modelling of thermal destruction of cylindrical shells with internal pre-pressure under laser irradiation, Comput. Struct. 71 (1999) 359–370.
[11] Z.P. Tang, Three-dimensional DEM theory and its application to impact mechanics, Sci. China 44 (6) (2001) 561–571.
[12] P. Geng, J.Z. Xing, X.X. Chen, Winding angle optimization of filament-wound cylindrical vessel under internal pressure, Arch. Appl. Mech. 87 (3) (2016) 365–384.
[13] M.D. Kashkoli, K.N. Tahan, M.Z. Nejad, Time-dependent thermomechanical creep behavior of FGM thick hollow cylindrical shells under non-uniform internal pressure, Int. J. Appl. Mech. 09 (06) (2017) 1750086.
[14] C. Li, T. Yao, X. He, et al., Stress analysis for the orthotropic pressurized structure of the cylindrical shell and spherical head, Thin-Walled Struct. 111 (2017) 29–37.
[15] M. Mirzaei, Failure analysis of an exploded gas cylinder, Eng. Fail. Anal. 15 (7) (2008) 820–834.
[16] K. Zondervan, D. Beck, Approximate closed-form expression for the probability of burst of a pressurized metal cylinder irradiated by a high-energy laser, in: Proceedings of the AIAA 33rd Plasmadynamics and Laser Conference, USA, 2002, Paper 2002-2220.
[17] L.A. Segel, C.C. Lin, Mathematics Applied to Deterministic Problems in the Natural Sciences, Macmillan, New York, 1974.
[18] Q.M. Tan, Dimensional Analysis With Case Studies in Mechanics, Springer-Verlag Berlin Heidelberg, Berlin, 2011.
[19] X.Q. Wu, Q.M. Tan, C.G. Huang, Geometrical scaling law for laser shock processing, J. Appl. Phys. 114 (2013) 043105.
[20] L. Liu, Y.W. Gui, Y.X. Du, et al., Study on the similarity criteria of aircraft structure temperature/stress/dynamic response, J. Therm. Sci. Technol. 7 (1) (2012) 262–271.
[21] S.L. Canfield, J. Peddieson, G. Garbe, Similarity criteria and associated design procedures for scaling solar sail systems, J. Spacecr. Rockets 48 (1) (2011) 218–221.
[22] Sh Torkamani, H.M. Navazi, A.A. Jafari, et al., Structural similitude in free vibration of orthogonally stiffened cylindrical shells, Thin-Walled Struct. 47 (11) (2009) 1316–1330.
[23] S. De Rosa, F. Franco, E. Ciappi, et al., Analysis of distorted similitudes for the frequency response of composite plates, Aerotec. Missili Spaz. 95 (1) (2016) 24–31.
[24] M.E. Asl, C. Niezrecki, J. Sherwood, et al., Vibration prediction of thin-walled composite I-beams using scaled models, Thin-Walled Struct. 113 (2017) 151–161.
[25] A.A. Yazdi, J. Rezaeepazhand, Applicability of small-scale models in prediction flutter pressure of delaminated composite beam-plates, Int. J. Damage Mech. 22 (4) (2013) 590–601.
[26] C.G. Huang, S.Y. Chen, Z.P. Duan, Similarity criterion about deformation and failure of pressurized cylinder subjected to laser irradiation, High Power Laser Part. Beams 16 (8) (2004) 962–966.
[27] Q.Y. Li, Damage Effects of Vehicles Irradiated by Intense Lasers, China Astronautic Publishing House, Beijing, 2012.